


# Single-stage spin-orbit Laguerre-Gaussian modal beam shaping from silica optics

Vagharshak Hakobyan<sup>1</sup>,<sup>1</sup> Keshaan Singh<sup>2</sup>,<sup>2</sup> Yuhao Lei,<sup>3</sup> Peter Kazansky,<sup>3</sup> Delphine Coursault,<sup>1</sup> Andrew Forbes,<sup>2</sup> and Etienne Brasselet<sup>1,\*</sup>

<sup>1</sup>*CNRS, Laboratoire Ondes et Matière d'Aquitaine, University of Bordeaux, F-33400 Talence, France*

<sup>2</sup>*School of Physics, University of Witwatersrand, 2000, Johannesburg, South Africa*

<sup>3</sup>*Optoelectronics Research Centre, University of Southampton, Southampton SO17 1BJ, United Kingdom*

 (Received 23 February 2024; revised 2 May 2024; accepted 3 May 2024; published 3 June 2024)

We report on the design, fabrication and performance of novel flat-optical spin-orbit modal beam shapers made from silica glass by femtosecond laser nanostructuring technology, choosing the Laguerre-Gauss basis as a case study. The basic design principle involves endowing a transparent dielectric material, initially isotropic and homogeneous, with doubly inhomogeneous anisotropic characteristics (optical axis orientation and birefringence). The quantitative structural characterization of the fabricated devices is achieved by Stokes polarimetric analysis and the modal beam shaping performance is assessed via modal decomposition. The modal beam shaping capabilities obtained outperform those of previously produced spin-orbit beam shapers based on the same fabrication technology. Also, current challenges and perspectives associated with high-order and spectrally broadband modal beam shaping are discussed. More generally, the proposed approach extends the scope of spin-orbit optical elements to any situation where complex field amplitude shaping is required in a single stage.

DOI: [10.1103/PhysRevApplied.21.064003](https://doi.org/10.1103/PhysRevApplied.21.064003)

## I. INTRODUCTION

The shaping of light, both in time and space, is a fundamental requirement of modern photonics technologies, today referred to as structured light [1]. In the spatial domain, the primary interest is in control over amplitude, phase, and polarization, for which a variety of technological solutions exist for on-demand control, already implemented in industrial and everyday applications. The controlled production and detection of families of orthogonal optical modes is of particular interest, for instance in the context of optical information, whatever the chosen basis set [2]. Starting with a given field, we need to transform its amplitude and phase so that they satisfy the condition for the existence of the desired mode. Considering the usual fundamental Gaussian beam as the field to be transformed into a distinct mode, this implies using a device imparting the required mode-specific field changes. Spatial light modulators enable this objective to be achieved digitally, based on amplitude-only [3] or phase-only [4] pixel-based control. Notably, these scalar diffractive approaches rely on selecting one of the diffraction orders as a drop port to modulate the amplitude. Still, this operation can also be performed using single-stage optical elements operating only in the zeroth-order diffraction channel, exploiting the

vector nature of light. This involves encoding the amplitude modulation in a given polarization state and filtering it by polarization projection using standard polarization optics. Such an approach was introduced theoretically a few years ago and illustrated in the context of the Laguerre-Gauss family of optical modes [5], although its generic nature makes it directly applicable to any other type of customized beam.

Single-stage complex amplitude (i.e., amplitude and phase) modulation based on polarization filtering involves the use of anisotropic and inhomogeneous optical elements. More precisely, the inhomogeneous character has both an orientation of the optical axis and a level of optical anisotropy. Their spatial distribution not only dictates the azimuth and ellipticity of the output polarization state, and thus the spatial distribution of amplitude modulation, but also the way in which the phase is spatially modulated. It should be noted that phase modulation has two origins, one dynamic, associated with wave propagation in the chosen medium, and the other geometric, associated with rotation of the optical axis in the plane of the optical element. Combining all these aspects, several implementations of the initial proposal [5] have been proposed and realized since then in the context of Laguerre-Gaussian beam shaping. They can be divided into two categories associated with the use of bulk- or surface-structured substrates. The first refers to attempts based on nanostructured silica glass [6,7], and the second

\*Corresponding author: [etienne.brasselet@u-bordeaux.fr](mailto:etienne.brasselet@u-bordeaux.fr)

to metallic [8] or dielectric [9–11] metasurfaces. Ultrafast laser direct writing techniques have been used to imprint nanogratings based birefringent modifications in silica glass for the fabrication of waveplates with spatially varying orientation of the optical axis [12]. More recently, birefringent modifications based on anisotropic nanopores in fused silica have been reported to realize optical elements with the advantage of enabling ultralow losses and continuous modulation of retardation [13]. Furthermore, these studies show that the nature of the polarization state of the drop port is more a matter of design choice than a requirement for achieving the desired optical transformation. Indeed, the experimental demonstrations were carried out indifferently in the case of a circularly [6–8,10] or linearly [9,11] polarized final state.

With the aim at contributing to the development of robust, durable, and large-aperture single-stage modal beam shaping optical elements exploiting the spin-orbit interaction of light, here we present advances of modal beam shapers made of laser nanostructured silica glass taking advantage of birefringent modifications based on anisotropic nanopores, and restricting to the particular case of Laguerre-Gauss modes. The latest experimental developments have not resolved the inherent drawback of the spatially variable birefringent phase delay, which involves taking into account a subsequent modulation of the dynamic phase which remains to be corrected [7]. We solve this issue by modifying previous designs and experimentally assess quantitatively the structural quality and the modal performances of the fabricated optical elements, which establishes a standard for the advent of spin-orbit modal beam shapers. Detailed experimental results are reported for a few low-order modes and monochromatic designs. Also, we discuss the extent to which the proposed approach allows us to deal with the generation of high-order and spectrally broadband Laguerre-Gaussian modes, which is supported by numerical and experimental results. This allows us to identify some avenues for future improvements and application perspectives.

## II. DESIGN AND FABRICATION

### A. Modal plate design

In this section, we summarize the basic knowledge relating to the definition of the optical characteristics of a spin-orbit modal beam shaper operating in the circular polarization basis and aiming at producing a given Laguerre-Gaussian beam from a normally incident circularly polarized fundamental Gaussian beam [5].

We start by recalling the expression for the electric field of Laguerre-Gaussian beams of azimuthal order  $l \in \mathbb{Z}$  and radial order  $p \in \mathbb{N}$  according to the paraxial expression for the electric field in the cylindrical coordinate system

$(r, \phi, z)$ , written as [14]

$$E_{l,p}(r, \phi, z; w_0) \propto \frac{w_0}{w(z)} \left[ \frac{r}{w(z)} \right]^{|l|} L_p^{|l|} \left( \frac{2r^2}{w(z)^2} \right) \times \exp \left[ -\frac{r^2}{w(z)^2} \right] \exp \left\{ i \left[ \frac{k_0 r^2 z}{2(z^2 + z_0^2)} + l\phi - (2p + |l| + 1) \arctan \left( \frac{z}{z_0} \right) \right] \right\} \quad (1)$$

for a beam propagating towards  $z > 0$ . Here,

$$L_p^{|l|}(x) = \sum_{m=0}^p \frac{(|l| + p)!}{(|l| + m)!(p - m)!m!} (-x)^m$$

where  $x = 2r^2/w(z)^2$ ,  $w(z) = w_0 \sqrt{1 + (z/z_0)^2}$ ,  $w_0$  is the beam waist radius,  $z_0 = k_0 w_0^2/2$  is the Rayleigh distance, and  $k_0 = 2\pi/\lambda$  is the wavevector in free space with  $\lambda$  being the wavelength. Note that the free-space propagation factor  $\exp(-i\omega t + ik_0 z)$  is omitted in Eq. (1).

Then we recall how the electric field of an incident circularly polarized paraxial beam is transformed by passing through a slab of inhomogeneous optically uniaxial medium, which is taken as lying in the  $(x, y)$  plane. The slab is defined as having its slow axis oriented at an angle  $\psi$  counted from the  $x$  axis and is associated with phase delays  $\Phi_{\text{slow}}$  and  $\Phi_{\text{fast}}$  for linearly polarized light along the slow and fast axes, respectively. We describe the incident field as  $\mathbf{E}_{\text{in}} = E_{\text{in}} \mathbf{c}_\sigma$ , where  $\mathbf{c}_\sigma = (\mathbf{x} + i\sigma \mathbf{y})/\sqrt{2}$  refers to the circular polarization Jones vector in the Cartesian coordinate system and  $\sigma = \pm 1$  refers to the field helicity. Neglecting diffraction through the slab, the optical transformation is described as a Jones matrix  $\hat{\mathbf{J}}$ ,

$$\mathbf{E}_{\text{out}} = \hat{\mathbf{J}} \mathbf{E}_{\text{in}}, \quad (2)$$

where  $\hat{\mathbf{J}}$  refers to a sequence of spatial rotations around the  $z$  axis and propagation along it,

$$\hat{\mathbf{J}} = \begin{pmatrix} \cos \psi & -\sin \psi \\ \sin \psi & \cos \psi \end{pmatrix} \begin{pmatrix} e^{i\Phi_{\text{slow}}} & 0 \\ 0 & e^{i\Phi_{\text{fast}}} \end{pmatrix} \times \begin{pmatrix} \cos \psi & \sin \psi \\ -\sin \psi & \cos \psi \end{pmatrix}. \quad (3)$$

Combining Eqs. (1)–(3), one obtains

$$\mathbf{E}_{\text{out}} = E_{\text{in}} e^{i\Phi_{\text{dyn}}} \left[ \cos(\Delta/2) \mathbf{c}_\sigma + i \sin(\Delta/2) e^{i\Phi_{\text{geo}}} \mathbf{c}_{-\sigma} \right] \quad (4)$$

where

$$\Delta = \Phi_{\text{slow}} - \Phi_{\text{fast}} \quad (5)$$

refers to the net birefringent phase delay experienced by light,

$$\Phi_{\text{dyn}} = (\Phi_{\text{slow}} + \Phi_{\text{fast}})/2 \quad (6)$$

refers to the helicity-independent *dynamic* phase, and

$$\Phi_{\text{geo}} = 2\sigma\psi \quad (7)$$

refers to the helicity-dependent *geometric* phase. Therefore, the contracircularly polarized ( $\mathbf{c}_{-\sigma}$ ) output polarization port can be used to impart an arbitrary complex amplitude modulation to an incident beam provided appropriately designed spatial distributions of  $\Delta$  and  $\psi$ .

In the present illustrative framework of Laguerre-Gauss beam shaping, the task is defined within a typical laboratory situation dealing with the transformation of an incident fundamental Gaussian beam with waist radius  $w_{\text{in}}$ ,  $\mathbf{E}_{\text{in}} = E_0 \exp(-r^2/w_{\text{in}}^2) \mathbf{c}_\sigma$ , into a Laguerre-Gauss beam of order  $(l, p)$ . The determination of the optical characteristics of the inhomogeneous and anisotropic medium is made according to the requirement  $E_{\text{out}} \propto E_{l,p}(r, \phi, z; w_{\text{out}})$ . Namely,

$$E_{\text{in}} \sin(\Delta/2) e^{i(\Phi_{\text{dyn}} + \Phi_{\text{geo}})} \propto E_{l,p}(r, \phi, z; w_{\text{out}}), \quad (8)$$

which can be satisfied by choosing

$$\Delta_{l,p}(r) = 2 \arcsin \left\{ \frac{|E_{l,p}(r, 0, 0; w_{\text{out}})| e^{r^2/w_{\text{in}}^2}}{\max \left[ |E_{l,p}(r, 0, 0; w_{\text{out}})| e^{r^2/w_{\text{in}}^2} \right]} \right\} \quad (9)$$

provided that  $w_{\text{out}} < w_{\text{in}}$ , and

$$\psi_{l,p}(r, \phi) = q\phi \pm \frac{\sigma}{2} \Phi_{\text{dyn}}(r) - \frac{\pi}{4} \left\{ 1 - \text{sign} \left[ L_p^{|l|} \left( \frac{2r^2}{w_{\text{in}}^2} \right) \right] \right\} \quad (10)$$

where  $q = n/2$  with  $n \in \mathbb{Z}$  and the  $\pm$  sign affects the way one can obtain a mode with  $l = 2\sigma q$  when  $\Phi_{\text{dyn}}$  is not a constant, which is the case in this work. Indeed, the laser-induced modifications of the optical anisotropy are not achieved at constant mean refractive index.

In this work, we choose a design with the  $-$  sign for Eq. (10), for which we obtain  $l = 2q$  for  $\sigma = +1$ , while the use of  $\sigma = -1$  implies flipping the modal plate upside down with respect to the  $z$  axis in order to obtain a mode associated with  $l = -2q$ . Also, we present modal results by using  $\sigma = +1$ , restricting our experimental investigations to the fundamental radial order  $p = 0$ . This leads to the following spatial profiles for the anisotropic features of

the modal plates:

$$\Delta_{l,0}(r) = 2 \arcsin \left\{ \left( \frac{r\sqrt{2}}{w_{\text{design}}} \right)^{|l|} \exp \left[ |l| \left( \frac{1}{2} - \frac{r^2}{w_{\text{design}}^2} \right) \right] \right\}, \quad (11)$$

and

$$\psi_{l,0}(r, \phi) = \frac{1}{2} [l\phi - \Phi_{\text{dyn}}(r)], \quad (12)$$

where the characteristic length  $w_{\text{design}}$  in Eq. (11) defines the incident beam waist radius maximizing the modal output power fraction up to the value  $|l|! e^{|l|}/(1 + |l|)^{1+|l|}$ . In addition, choosing  $w_{\text{in}} = w_{\text{design}}$  leads to an output waist radius for the modal beam  $w_{\text{out}} = w_{\text{design}}/\sqrt{1 + |l|}$ . Still, as previously noted [10], the pure modal nature is not altered when  $w_{\text{in}} \neq w_{\text{design}}$ , at least for  $p = 0$ , but is associated with another waist value given by

$$w_{\text{out}} = \frac{w_{\text{design}}}{\sqrt{|l| + w_{\text{design}}^2/w_{\text{in}}^2}}. \quad (13)$$

## B. Modal plate fabrication

The space-variant anisotropic optical elements were fabricated by femtosecond laser processing of synthetic silica glass substrates. This was carried out with a mode-locked regeneratively amplified femtosecond laser system (PHAROS, Light Conversion Ltd.), which delivered optical pulses with 600 fs duration at 1030 nm wavelength, with a repetition rate of 200 kHz. Laser pulses were focused with a 0.16 numerical aperture aspheric lens beneath the surface of the substrate that was fixed on a three-axial air-bearing translation stage. This enabled the controlled generation of anisotropic nanopore assemblies, imparting form birefringence to the initially optically isotropic medium with low scattering losses [13,15]. All of the fabricated devices reported in the present work were manufactured according to this approach, which provides optical elements having damage threshold of about 1.6 J/cm<sup>2</sup> for a 1030-nm, 300-fs incident laser beam, which is comparable to pristine silica glass, as reported in [16]. The direction of the laser-induced slow axis is perpendicular to the polarization direction of the writing beam, which was controlled by a combination of a polarizer, a Pockels cell and a quarter waveplate. Moreover, the magnitude of the birefringence was controlled by adjusting the pulse energy from 650 nJ to 850 nJ, which allowed continuous and monotonous control of the optical path difference (or anisotropic retardance)  $\delta = (\Phi_{\text{slow}} - \Phi_{\text{fast}})/k_0$  from 1 nm to 40 nm for the chosen operating wavelength  $\lambda_0 = 532$  nm. The maximal retardance of 266 nm expected from Eq. (11) was achieved by piling up several layers of laser-induced modifications.

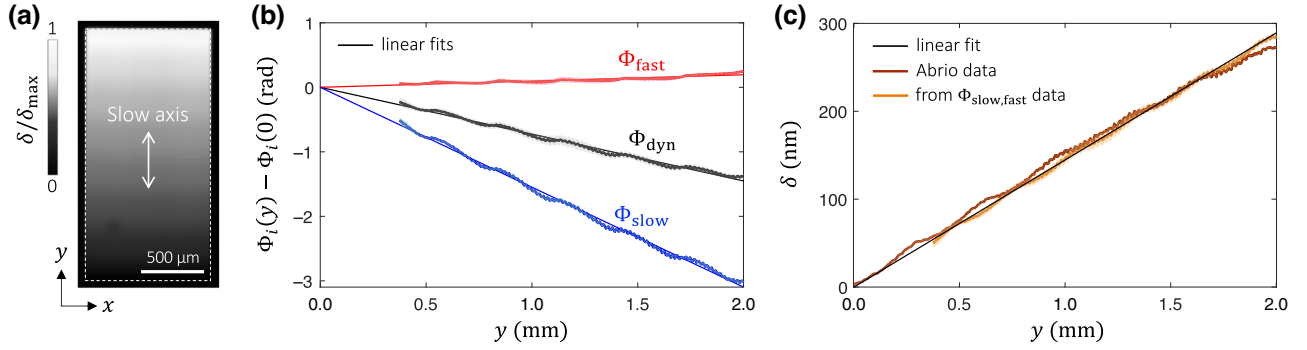


FIG. 1. (a) Normalized anisotropic retardance of the calibration sample retrieved from Abrio imaging system. (b) Measured fast phase  $\Phi_{\text{fast}}$  (red curve), slow phase  $\Phi_{\text{slow}}$  (blue curve), and the associated dynamic phase  $\Phi_{\text{dyn}} = (\Phi_{\text{slow}} + \Phi_{\text{fast}})/2$  (black curve) along the  $y$  direction of the sample. (c) Anisotropic retardance  $\delta$  along the  $y$  direction of the sample measured from Abrio imaging system (brown curve) and from wavefront sensor phase measurements as  $\delta = (\Phi_{\text{slow}} - \Phi_{\text{fast}})/k_0$  (orange curve). For all plots: lines refer to linear fit, curves refer to mean value evaluated over the 1-mm-wide side of the sample along the  $x$  direction and light-color areas refer to  $\pm$  standard deviation around the mean value.

To date, previous works dealing with silica-based modal shapers have all overlooked the dynamic phase issue, which prevents pure Laguerre-Gauss modes from being obtained [6,7]. Here we lifted this limitation by determining the relationship between  $\Phi_{\text{slow}} - \Phi_{\text{fast}}$  and  $\Phi_{\text{slow}} + \Phi_{\text{fast}}$ . This was ascertained from the characterization of a 1 mm  $\times$  2 mm rectangular calibration sample exhibiting a linearly varying anisotropic retardance along one direction [see Fig. 1(a)]. Using a wavefront sensor operating at 550 nm wavelength (SID4-HR, Phasics) we measured the slow and fast phase changes with respect to untreated silica,  $\Phi_{\text{slow,fast}}(y) - \Phi_{\text{slow,fast}}(0)$ , in the direction of the  $y$  axis along which  $\delta$  varies, [see Fig. 1(b)]. This allowed evaluation of the dynamic phase  $\Phi_{\text{dyn}}$  [Fig. 1(b)] and the anisotropic retardance  $\delta$  [Fig. 1(c)]. A complementary measurement made using an Abrio imaging system (CRi, Inc.) operating at 546 nm wavelength quantitatively agrees with the phase measurements [see Fig. 1(c)]. From the linear fit of  $\Phi_{\text{dyn}}$  versus  $y$  and that of both datasets for  $\delta$ , we experimentally establish the linear relationship

$$\Phi_{\text{dyn}} \simeq -0.46k_0\delta = -0.46\Delta. \quad (14)$$

Laguerre-Gaussian modal plates with  $l = (1, 2, 3)$ , 1 mm diameter and 127 DPI resolution were manufactured according to Eqs. (11) and (12), using  $w_{\text{design}} = 250 \mu\text{m}$  and disk-shaped structured area with diameter  $2R = 1 \text{ mm}$ . A second set of optical elements, not taking into account the dynamic phase correction in Eq. (12), were also produced in order to quantitatively assess the need to take the dynamic phase issue into account.

### III. MODAL PLATE CHARACTERIZATION

The fidelity of the fabricated optical elements with respect to the design was assessed by polarimetric imaging using the setup sketched in Fig. 2(a). Measurement of

Stokes parameters at the output of the sample was done by reimaging the sample on a camera and performing projective measurements using a polarization controller. We chose  $\lambda_{\text{probe}} = 633 \text{ nm}$  as the wavelength of the circularly polarized probe light having helicity  $\sigma_{\text{probe}}$ . This prevented a phase wrapping ambiguity since the maximal birefringent phase delay is  $\pi$  at 532 nm, hence less at 633 nm. Specifically, the retardance  $\delta$  and the orientation angle  $\psi$  were obtained from the measured reduced Stokes vector  $\mathbf{s} = (s_1, s_2, s_3)$  [17] according to

$$\delta = \frac{\lambda_{\text{probe}}}{2\pi} \arccos(\sigma_{\text{probe}}s_3), \quad (15)$$

which implies assuming negligible dispersion of the optical anisotropy, and

$$\psi = \frac{1}{2} \arctan\left(\frac{s_2}{s_1}\right) - \sigma_{\text{probe}}\frac{\pi}{4}. \quad (16)$$

The results are shown in Fig. 2(b) where the displayed raw data show the pixelated nature of the optical elements, here a modal plate with  $l = 1$ . This figure also shows a smoothed version of the experimental maps that will further facilitate the visual comparison between experimental and simulated data, the latter being made using a continuous design.

A summary of the polarimetric analysis for the two sets of three plates is shown in Fig. 3, where the optical elements that take dynamic phase correction into account are designated as “corrected,” while those that do not are designated as “uncorrected.” This leads to the conclusion that, overall, the manufacturing protocol is satisfactory, at least in terms at a qualitative level. Still, Stokes polarimetric analysis also allows us to go beyond a qualitative assessment, which we report in Fig. 4. There, the experimental azimuthal profile of the slow axis orientation angle (left

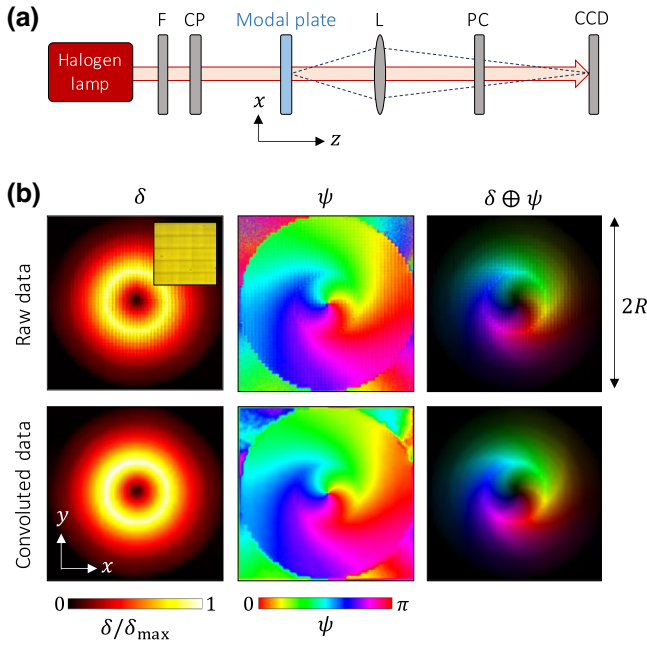


FIG. 2. (a) Experimental setup for full Stokes polarimetric analysis of the modal plates at 633 nm wavelength. F, spectral filter for 633 nm wavelength; CP, circular polarizer; L, imaging lens (4 $\times$  microscope objective with numerical aperture NA = 0.1); PC, polarization controller allowing charged coupled device (CCD) camera recording of the intensity distribution of the output field projected on an arbitrary polarization state. (b) Maps of the anisotropic optical features in the  $(x, y)$  plane for the corrected modal plate with  $l = 1$ . Left column: retardance ( $\delta$ ). Middle column: slow axis orientation angle ( $\psi$ ). Right column: combination of retardance and orientation ( $\delta \oplus \psi$ ) for which the brightness refers to  $\delta/\delta_{\max}$  and the hue colormap refers to  $\psi$ . Top row: raw data of the pixelated plate where the inset refers to the bright field image of a  $5 \times 5$  pixel area, each pixel having  $20 \mu\text{m} \times 20 \mu\text{m}$  area. Bottom row: convolution smoothing of raw data over one pixel.

column) and the radial profile of the retardance (middle column) extracted from the reconstructed maps presented in Fig. 3 are shown and compared to the expected behavior (red curves) for both uncorrected and corrected modal plates. The radial profile of the slow axis orientation angle correction  $d\psi = \psi - l\phi/2$  for the corrected modal plates is also shown (right column).

These results demonstrate a good level of fidelity in the laser writing of orientation features. Still, we note an apparent difficulty in reproducing the cusp profile associated with both the retardance and the dynamic phase correction via geometric phase management. In fact this is due more to the pixelation chosen for fabrication and the azimuth average assessment than to any inherent limitation of the laser nanostructuring process. Now that the structure of the modal plates is validated, we address their modal characteristics in the next section.

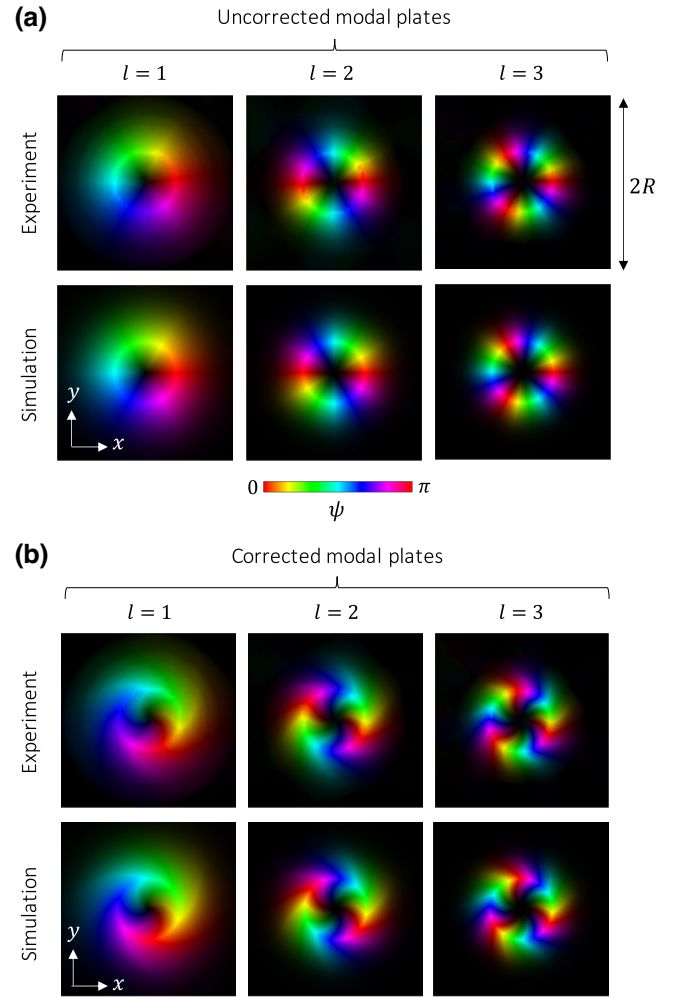


FIG. 3. Structural maps in the  $(x, y)$  plane combining retardance (brightness) and orientation (color) for (a) uncorrected and (b) corrected modal plates with  $l = (1, 2, 3)$ . Top row: experimental convoluted data. Bottom row: simulations.

## IV. MODAL PROPERTIES

### A. Beam propagation

A salient but nonexclusive characteristic pertaining to Laguerre-Gaussian modes is that their shape is unaltered, up to a spatial stretching factor, as they propagate through a linear and homogeneous medium. Experimentally, this can be grasped by recording the transverse intensity distribution as the beam propagates. The experiment is done by preparing an incident circularly polarized Gaussian laser beam with  $w_{\text{in}} = w_{\text{design}}$  and imaging the contracircularly polarized spatial intensity distribution of the beam at a distance  $z$  from the sample in 5-mm steps and choosing a 1 : 1 imaging condition. This was realized by translating an objective lens together with a camera, in front of which is placed a circular polarizer, while keeping the distance between them fixed. Azimuth-averaged radial intensity profiles were then calculated from the recorded images,

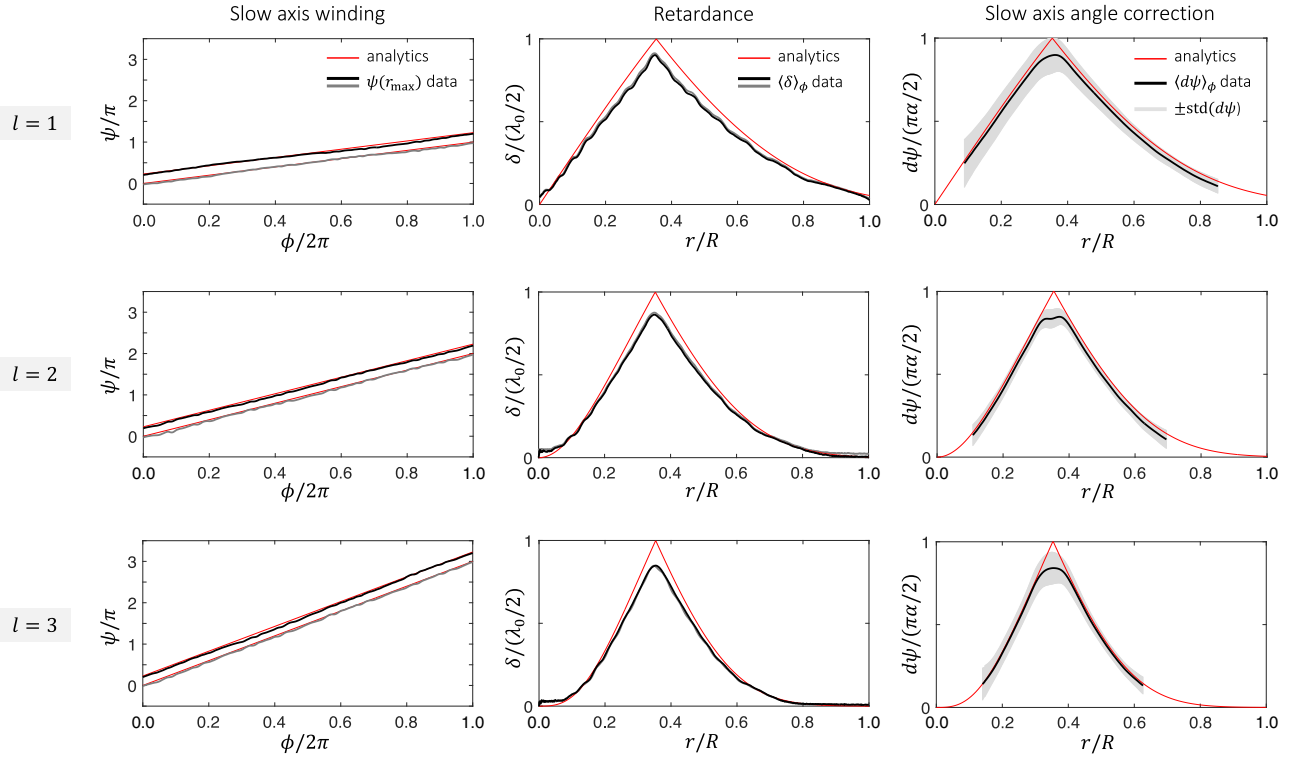


FIG. 4. Theoretical and experimental profiles of the azimuthal dependence of the slow axis orientation angle evaluated at  $r_{\max}$  defined as  $\delta(r_{\max}) = \max_r[\delta(r)]$  (left column), the azimuth-averaged radial profile of the retardance  $\langle\delta\rangle_\phi$  (middle column) and the azimuth-averaged radial profile of the slow axis orientation angle correction  $\langle d\psi\rangle_\phi$  for the corrected modal plates (right column) for  $l = (1, 2, 3)$ . The retardance and slow axis orientation angle correction profiles are normalized to their maximal theoretical value  $\lambda/2$  and  $\pi\alpha/2$ , respectively, where  $\alpha \simeq 0.46$  is the proportionality factor between  $\Phi_{\text{dyn}}$  and  $\Delta$  [see Eq. (14)]. Thin red curves: analytics. Thick gray/black curves: experimental data from uncorrected/corrected modal plates.

which allowed a meridional intensity cross-section to be reconstructed.

The results are shown in Fig. 5 for  $l = 1$  and three types of optical elements. In this case, the standard vortex plate refers to a  $q$ -plate design [18], which here corresponds to  $\Delta = \pi$  and  $\psi = \phi/2$  and has been fabricated using the same laser nanostructuring technique as the other plates. For the latter plate we obtain the well-known ringing intensity profile [19], which is associated with the presence of a distribution of radial modes with  $p \neq 0$  [20]. As expected, the invariance of the beam shape upon propagation is visually optimized for the corrected modal plate, whereas the results for uncorrected modal plates highlight the aspheric focusing associated with the spatial modulation of the dynamic phase. Quantitatively we make use of the  $L_2$ -norm to define a mean-square distance  $d$  between two real functions  $f(x)$  and  $g(x)$  in the range  $x \in [a, b]$  as  $d(f, g) = \int_a^b [f(x)^2 - g(x)^2]^2 dx$ . We thus define the dimensionless quantity

$$\epsilon_{l,p}(z) = \frac{\int_0^{R_{\max}} [I_{\text{plate}}(r, z) - I_{L_{G_{l,p}}}(r, z)]^2 dr}{\int_0^{R_{\max}} I_{L_{G_{l,p}}}(r, z)^2 dr} \quad (17)$$

as an estimate of the relative overall deviation with respect to a pure Laguerre-Gauss mode with orders  $(l, p)$ , where  $R_{\max} = 500 \mu\text{m}$  is the maximal distance from the  $z$  axis from which the intensity profile is measured. The results are shown in Fig. 6 for  $(l, p) = (1, 0)$ , which ascertains that the corrected plates outperforms with respect to previous experimental realizations [6,7].

## B. Modal purity

The detailed determination of the modal performance of the fabricated silica optical elements is done by assessing the modal content of the generated field at the output of the modal plates,

$$\tilde{E}_{\text{out}}(r, \phi, 0) = \sum_{l,p} c_{l,p} \tilde{E}_{l,p}(r, \phi, 0; w_{\text{out}}), \quad (18)$$

where the tilde symbol refers to normalized fields that satisfy  $\iint |\tilde{E}|^2 r dr d\phi = 1$ ,  $w_{\text{out}}$  is the targeted Laguerre-Gauss waist radius given by Eq. (13), and the complex coefficients  $c_{l,p}$  tell us about the modal content of the field. In particular, noting that  $\sum_{l,p} |c_{l,p}|^2 = 1$ ,  $|c_{l,p}|^2$  represents the power fraction carried by the basis element with

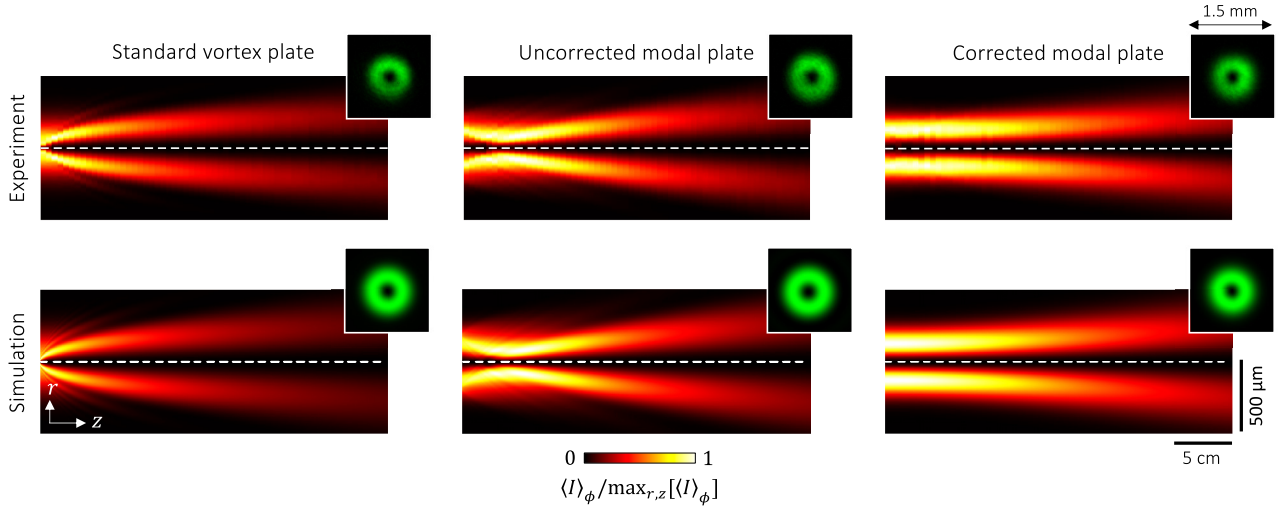


FIG. 5. Experimental (top row) and simulated (bottom row) normalized azimuth-average intensity distribution in the  $(z, r)$  plane for standard vortex plate (left column), uncorrected (middle column), and corrected (right column) modal plates for  $l = 1$ . The experimental data are recorded by moving a fixed system made of a lens, a circular polarizer and a camera, along the  $z$  (dashed line) axis in steps of 5 mm over a distance of 30 cm. Insets: transverse intensity distribution recorded at  $z = 30$  cm. The simulation is made using the Fourier beam propagation method.

indices  $(l, p)$ . Experimentally, we determine the modal content using a well-established modal decomposition approach based on the use of a spatial light modulator [21]. Accordingly, we used the setup depicted in Fig. 7(a), preparing an incident circularly polarized Gaussian laser beam with  $w_{\text{in}} = w_{\text{design}}$ . The output field  $\tilde{E}_{\text{out}}$  was then imaged on a digital micromirror device (DMD) using a  $4f$  imaging system. Following [22], the DMD encoded an amplitude hologram that makes the field of the first diffraction order proportional to  $\tilde{E}_{\text{out}}\tilde{E}_{l,p}^*$ . Then we operated an optical Fourier transform of the first diffraction order by using a lens and placing the camera at the Fourier plane, where the intensity distribution is given by

$$I_{\text{Fourier plane}}(\boldsymbol{\kappa}) \propto \left| \iint \tilde{E}_{\text{out}}\tilde{E}_{l,p}^* \exp(i\boldsymbol{\kappa} \cdot \mathbf{r}) r dr d\phi \right|^2, \quad (19)$$

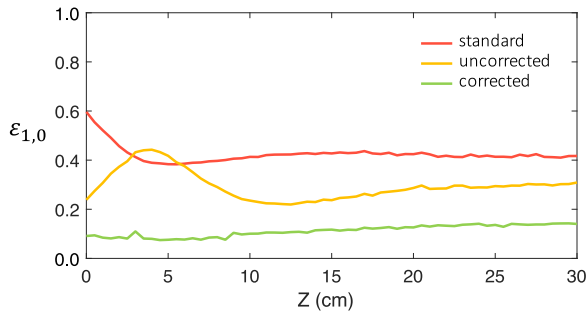


FIG. 6. Experimental  $L_2$ -norm relative mean square distance between the measured radial intensity profiles for standard, uncorrected, and corrected vortex plates with  $l = 1$  and that of a Laguerre-Gauss mode  $\text{LG}_{1,0}$  versus the propagation distance  $z$ , where  $z = 0$  refers to the plane of the plate.

in which  $\boldsymbol{\kappa}$  refers to the spatial frequencies wavevector in the Fourier plane. Therefore, accounting for the orthonormal nature of the Laguerre-Gauss basis  $\{\tilde{E}_{l,p}\}$ , we get

$$I_{\text{Fourier plane}}(\mathbf{0}) \propto |c_{l,p}|^2 \quad (20)$$

for the on-axis intensity in the Fourier plane. We choose a square region of  $3 \times 3$  pixels centered on-axis to evaluate  $I_{\text{Fourier plane}}(\mathbf{0})$ , and record the outcome via a power measurement, taking care to select the optimal output beam waist for the modal decomposition [23], that is,  $w_{\text{out}} = w_{\text{design}}/\sqrt{1 + |l|}$  [24], and whose expression is experimentally validated by determining the output beam waist value that maximizes  $|c_{l,0}|^2$ . The hologram encoded on the DMD is then iteratively refreshed to achieve all-optical projection of the output field over a range of Laguerre-Gaussian modes given  $\{l, p\} = \{-5 \leq l \leq 5, 0 \leq p \leq 5\}$  and the measured powers are eventually normalized to satisfy the completeness condition  $\sum_{\{l,p\}} |c_{l,p}|^2 = 1$ .

The results are summarized in Fig. 7(b), where the mean values and standard deviations shown refer to six (12) independent measurements [three (six) for each value of  $\sigma = \pm 1$ ] for standard (uncorrected) plates. Indeed, we recall that these designs are equally functional whatever the incident spin state provided that the contracircular polarization state is selected for the uncorrected plates. In addition, the data refer to six independent measurements for  $\sigma = 1$  for the corrected plates. This quantitatively ascertains the enhanced modal performance of the corrected modal plates compared to the other designs. Still, since both amplitude and phase are controlled in the corrected case one would expect 100% purity whatever  $l$ ,

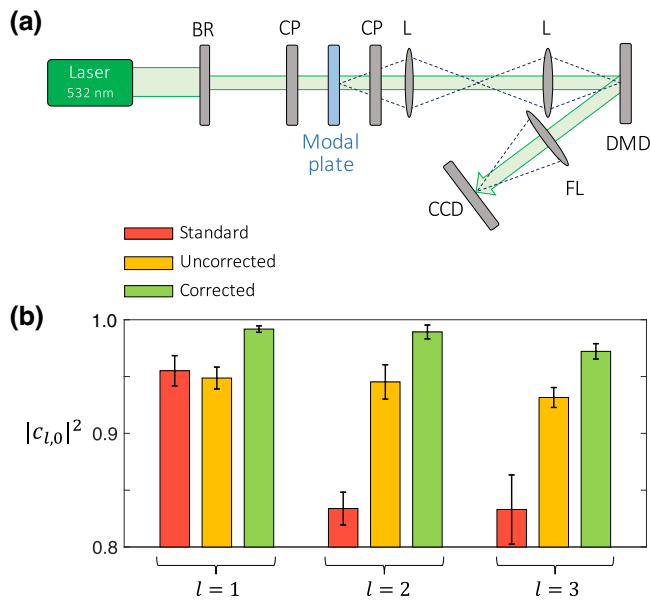


FIG. 7. (a) Experimental arrangement used to perform modal decomposition. BR, beam reducer made of a pair of lenses with focal lenses 275 mm and 100 mm; CP, circular polarizer; L, pair of lenses with focal length 150 mm used in  $4f$  configuration; DMD, digital micromirror device ( $1080 \times 1920$  pixels, each  $7.6 \mu\text{m} \times 7.6 \mu\text{m}$  in size); FL, Fourier lens with focal length 500 mm; CCD, intensity recording device ( $1288 \times 924$  pixels, each  $3.75 \mu\text{m} \times 3.75 \mu\text{m}$  in size). (b) Experimentally measured modal power fractions  $|c_{l,0}|^2$  of the three kinds of beam shapers studied in this work for  $l = (1, 2, 3)$ , using the appropriate input spin state for the corrected modal plates.

up to a decrease in efficiency with increasing  $|l|$ . However, we recall that the modal purity is ideally 100% for continuous devices only. Dealing with experiments and pixelated devices, it is not surprising that the performance does not reach that of ideal continuous patterned devices. As for the observed decrease with the order of the plate, we note that we chose a fixed pixelation regardless of  $l$ , in practice, and that the radial profiles for  $\Delta$  and  $\psi$ , are steeper as  $|l|$  increases. Therefore, the effect of pixelation becomes more significant for larger  $|l|$ , which gives a credible understanding of the observed trend.

## V. DISCUSSION

### A. Toward high-order modes

The full exploitation of high-dimensional bases for light in optical information and communication relies on the technological ability to design devices capable of generating high-order modes. Notably, the generation of Laguerre-Gaussian modes with high indices comes with a fabrication challenge due to the increase in spatial frequencies as  $l$  and  $p$  increase. Still, advances in nanofabrication make it possible to achieve it from cascaded [24,25] or

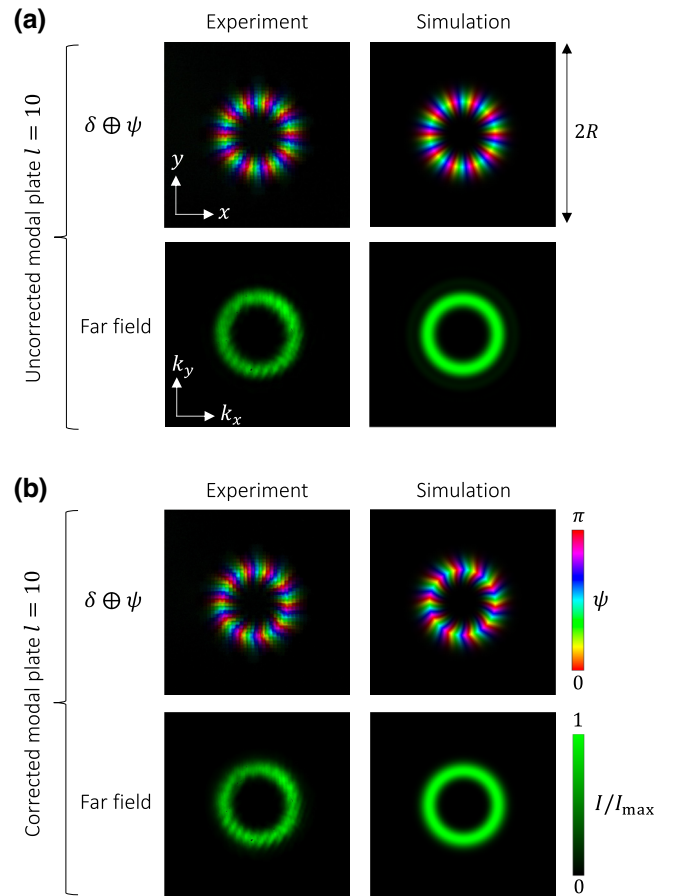


FIG. 8. Structural maps in the  $(x, y)$  plane combining retardance (brightness) and orientation (color) and far-field intensity distribution for (a) uncorrected and (b) corrected modal plates with  $l = 10$ . Left column: experimental data. Right row: simulation from ideal design.

single-stage [11] metasurfaces. Regarding laser nanostructured silica optics, although the generation of light beams with high orbital angular momentum states ( $l \sim 100$ ) has been reported, it remains limited to nonmodal standard plates. Here we explore the possible extension of the modal approach to high-order Laguerre-Gaussian modes, by choosing the case study  $(l, p) = (10, 0)$ . Our results are shown in Fig. 8 both for uncorrected and corrected designs, keeping the same parameters as for the demonstration for  $l = (1, 2, 3)$ , namely  $w_{\text{in}} = 250 \mu\text{m}$ ,  $2R = 1 \text{ mm}$ , and a structured pixel size of  $20 \mu\text{m} \times 20 \mu\text{m}$  as done for low-order modes. Although the intensity distribution is qualitatively satisfactory, the present pixelated design of the modal plates and their limited size does not allow high values to be attained for the measured modal power fractions with our optical system. In addition, while the uniform design exhibits less than 1% according to previous work [13], the pixelated devices have typical scattering losses of the order of 5%. This makes design improvements desirable when dealing with high-order modal plates.



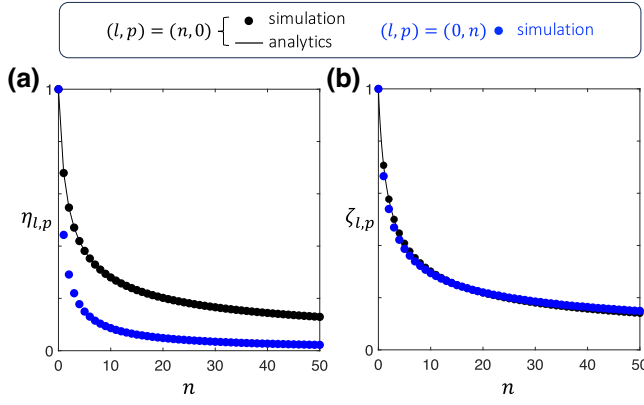


FIG. 9. Influence of the azimuthal and radial indices on the modal beam shaping characteristics for corrected modal plates with the use of the appropriate input spin state. (a) Calculated modal conversion efficiency,  $\eta_{l,p}$  and (b) the corresponding normalized beam waist for the Laguerre-Gauss modal decomposition,  $\zeta_{l,p} = w_{\text{out}}/w_{\text{design}}$ . Black color:  $0 \leq l \leq 50$  at  $p = 0$ . Blue color:  $0 \leq p \leq 50$  at  $l = 0$ . All data are evaluated at the nominal wavelength and using  $w_{\text{in}} = w_{\text{design}}$ . An analytical solution exists for  $p = 0$ , which gives  $\eta_{l,0} = |l! e^{|l|} / (1 + |l|)^{1+|l|}$  and  $\zeta_{l,0} = (1 + |l|)^{-1/2}$  [5].

It is noteworthy that in the single-stage strategy framework, the generation of high-order modes faces an issue which remains unsolved even in the limit of ideal spatial resolution. The expected output optical power fraction that corresponds to the  $(l, p)$  mode,

$$\eta_{l,p} = \frac{4}{w_{\text{in}}^2} \int_0^\infty \sin^2 [\Delta_{l,p}(r)/2] \exp(-2r^2/w_{\text{in}}^2) r dr, \quad (21)$$

indeed drastically decreases with the mode order, as shown in Fig. 9 for  $(l, p) = (n, 0)$  or  $(0, n)$ , up to  $n = 50$ . In this

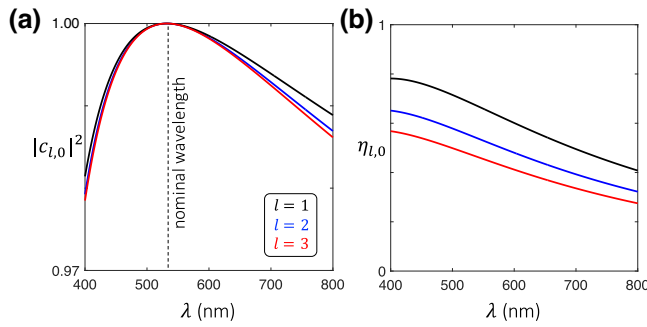


FIG. 10. Influence of a detuned incident wavelength on the modal performance for corrected modal plates with  $l = (1, 2, 3)$  using the appropriate input spin state. (a) Calculated modal power fractions  $|c_{l,0}|^2$  and (b) the corresponding modal power conversion efficiencies  $\eta_{l,p}$ . All data are evaluated using  $w_{\text{in}} = w_{\text{design}}$  and  $w_{\text{out}} = w_{\text{design}}/\sqrt{1 + |l|}$  for the Laguerre-Gauss modal decomposition at the nominal wavelength  $\lambda_0 = 532$  nm, for which the plate is monomode.

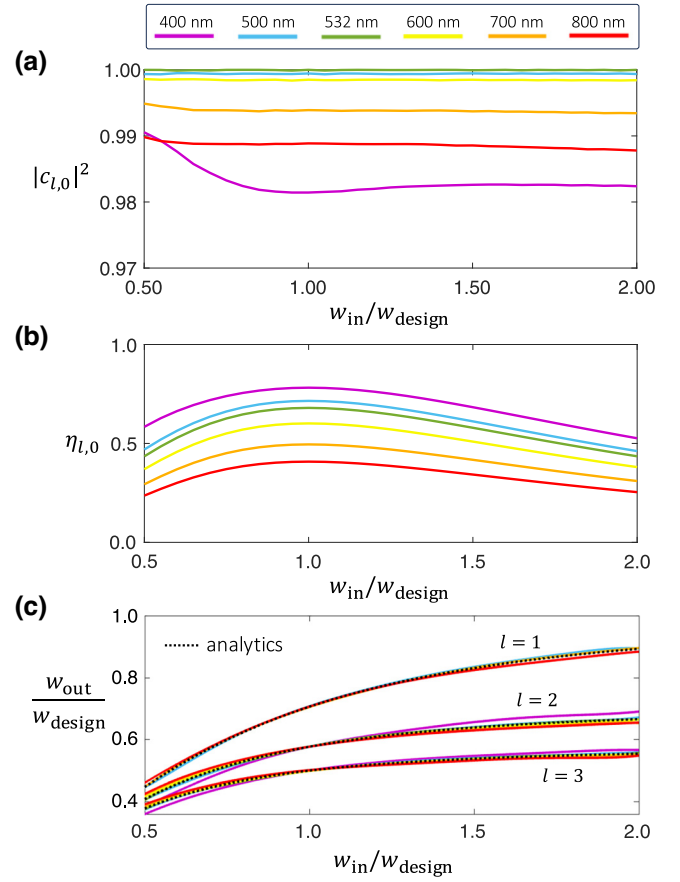


FIG. 11. Influence of a detuned incident beam waist on the modal performance across the visible domain (color curves) for corrected modal plates using the appropriate input spin state. (a) Calculated modal power fractions  $|c_{l,0}|^2$  and (b) the corresponding modal conversion efficiencies  $\eta_{l,0}$  for  $l = 1$ . (c) Calculated normalized output beam waist  $w_{\text{out}}/w_{\text{design}}$  that corresponds to (a) and (b) extended to  $l = (1, 2, 3)$ , where the dotted black curves refer to analytical results [Eq. (13)] at the nominal wavelength  $\lambda_0 = 532$  nm.

figure we also report on the corresponding output beam waist, which recalls the importance of selecting the proper “ruler” when performing modal decomposition analysis, not only for minimizing the number of modes that describe a given light beam. To date, there is no way to remedy this limitation.

## B. Robustness to spectral and waist detuning

So far, we have explored modal performance by selecting nominal values for the wavelength and the input beam waist in relation to the chosen design. Here we numerically address the question of the extent to which detuning is detrimental to the modal performance of the fabricated optical element. On the one hand, the consequences of a spectral detuning at the nominal input beam waist in terms of modal purity and modal power conversion efficiency are shown in Fig. 10 for  $l = (1, 2, 3)$  and  $p = 0$ . It appears

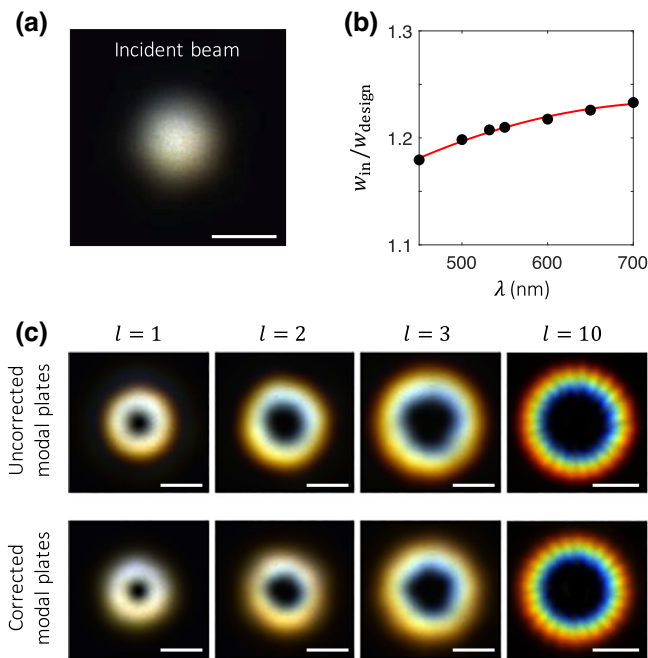


FIG. 12. Experimental supercontinuum modal beam shaping. (a) Intensity profile of the incident beam. Markers: experimental data. Solid curve: guide for the eye. (b) Dependence of the normalized incident beam waist on the wavelength in the visible domain. The intensity profile of the shaped beam after 20 cm propagation are shown in (c) for uncorrected and corrected modal plates, for  $l = (1, 2, 3, 10)$  and  $p = 0$ . Scale bars: 1 mm for  $l = 10$ , otherwise 400  $\mu\text{m}$ .

that a modal plate designed for a wavelength of 532 nm exhibits only a slight decrease in performance regarding its purity, which is a typical feature of geometric phase optical elements, with  $|c_{l,0}|^2 > 0.98$  over the whole visible range up to the near infrared. In contrast, the amount of processed light typically decreases by a factor of 2 over the visible domain, which suggests practical limitations whenever photon flux is an issue. On the other hand, the resilience of modal plate performance with respect to detuning of the incident beam waist is very good whatever the wavelength detuning, as shown in Figs. 11(a) and 11(b). In addition, our numerical investigations show that Eq. (13), which describes the optimal choice for the output beam waist versus the incident one as far as the modal decomposition is concerned, can be used as a rule of thumb over a broad range of wavelengths around the nominal [see the dotted analytical curve in Fig. 11(c)].

These results therefore suggest that broadband spin-orbit modal beam shaping can be achieved, at least at a good approximation. This is qualitatively explored experimentally by using an incident circularly polarized supercontinuum laser beam whose waist variation over the visible domain is no larger than a few percent [see Figs. 12(a)

and 12(b)]. The experiments are done for both the uncorrected and the corrected modal plates [see Fig. 12(c)], for which we used achromatic quarter-wave plates and a polarizer for achieving circular polarization projections at the input and output of the optical element. The observed color dispersion along the radial coordinate, which is all the more pronounced as the order of the mode increases, is due to the conjunction of at least two factors: first, the wavelength typically varies by a factor of 2 in the visible domain, thus leading to substantially larger beam divergence in the red than in the blue parts of the spectrum, recalling that the incident beam waist is almost independent of wavelength; and second, the relative “thickness” of a doughnut-shaped intensity profile of a vortex beam decreases with its topological charge  $l$ , thus enhancing any radial dispersion effects.

## VI. CONCLUSION

Present advances in the design and fabrication of spin-orbit modal plates made of laser nanostructured silica glass contribute to recent efforts devoted to single-stage modal beam shaping strategies [5–11], which might eventually seed the emergence of applications where compact solutions for complex amplitude shaping are needed. In particular, the use of silica optics with macroscopic clear aperture can lend a valuable robustness to the photon flux that can process a high-power laser beam that does not require power amplification, the latter remaining a nontrivial task to date [26]. The relative insensitivity of the modal performance to the input beam characteristics (wavelength, waist radius) is another remarkable asset of the optical elements developed. Importantly, the inherent issue related to the spatial modulation of the dynamic phase prevents fully taking advantage of the key spin-orbit interaction feature that involves spin-controlled wavefront reversal. The right/left symmetry is indeed broken by design as discussed in Sec. II A. Although spatially modulated form birefringence comes with spatial modulation of the dynamic phase, a compensation approach based on bilayer structuring has been suggested [27], though not yet investigated experimentally. Another limitation requiring further work is associated with the substantial decrease in modal power conversion efficiencies as the mode order increases.

## ACKNOWLEDGMENTS

E.B. and D.C. acknowledge support from the French National Research Agency (ANR-21-CE24-0014-01), the Wits-CNRS 2021 PhD joint program, and the IdEx University of Bordeaux/Grand Research Program GPR LIGHT. P.K. acknowledges support from the European Research Council (ENIGMA, 789116).

- [1] A. Forbes, M. de Oliveira, and M. R. Dennis, Structured light, *Nat. Photon.* **15**, 253 (2021).
- [2] M. Chen, K. Dholakia, and M. Mazilu, Is there an optimal basis to maximise optical information transfer? *Sci. Rep.* **6**, 22821 (2016).
- [3] V. Arrizón, G. Méndez, and D. Sánchez-de La-Llave, Accurate encoding of arbitrary complex fields with amplitude-only liquid crystal spatial light modulators, *Opt. Express* **13**, 7913 (2005).
- [4] A. Forbes, A. Dudley, and M. McLaren, Creation and detection of optical modes with spatial light modulators, *Adv. Opt. Photon.* **8**, 200 (2016).
- [5] M. Rafayelyan and E. Brasselet, Laguerre-Gaussian modal q-plates, *Opt. Lett.* **42**, 1966 (2017).
- [6] M. Rafayelyan, T. Gertus, and E. Brasselet, Laguerre-Gaussian quasi-modal q-plates from nanostructured glasses, *Appl. Phys. Lett.* **110**, 261108 (2017).
- [7] D. Coursault and E. Brasselet, Nanostructured silica spin-orbit optics for modal vortex beam shaping, *Nanophotonics* **11**, 805 (2022).
- [8] H. Mao, Y.-X. Ren, Y. Yu, Z. Yu, X. Sun, S. Zhang, and K. K. Wong, Broadband meta-converters for multiple Laguerre-Gaussian modes, *Photonics Res.* **9**, 1689 (2021).
- [9] M. Piccardo and A. Ambrosio, Arbitrary polarization conversion for pure vortex generation with a single metasurface, *Nanophotonics* **10**, 727 (2021).
- [10] M. Jin, B. Sanchez-Padilla, X. Liu, Y. Tang, Z. Hu, K. Li, D. Coursault, G. Li, and E. Brasselet, Spin-orbit modal optical vortex beam shaping from dielectric metasurfaces, *Adv. Opt. Mater.* **12**, 2202149 (2022).
- [11] M. de Oliveira, M. Piccardo, S. Eslami, V. Aglieri, A. Toma, and A. Ambrosio, Radially and azimuthally pure vortex beams from phase-amplitude metasurfaces, *ACS Photonics* **10**, 290 (2023).
- [12] M. Beresna, M. Gecevičius, P. G. Kazansky, and T. Gertus, Radially polarized optical vortex converter created by femtosecond laser nanostructuring of glass, *Appl. Phys. Lett.* **98**, 201101 (2011).
- [13] M. Sakakura, Y. Lei, L. Wang, Y.-H. Yu, and P. G. Kazansky, Ultralow-loss geometric phase and polarization shaping by ultrafast laser writing in silica glass, *Light Sci. Appl.* **9**, 1 (2020).
- [14] A. E. Siegman, *Lasers* (University Science Books, Melville, NY, USA, 1986).
- [15] Y. Lei, H. Wang, G. Shayeganrad, and P. G. Kazansky, Ultrafast laser nanostructuring in transparent materials for beam shaping and data storage, *Opt. Mater. Express* **12**, 3327 (2022).
- [16] G. Shayeganrad, X. Chang, H. Wang, C. Deng, Y. Lei, and P. G. Kazansky, High damage threshold birefringent elements produced by ultrafast laser nanostructuring in silica glass, *Opt. Express* **30**, 41002 (2022).
- [17] M. Born and E. Wolf, *Principles of Optics* (Cambridge University Press, Cambridge, England, 2019).
- [18] L. Marrucci, C. Manzo, and D. Paparo, Optical spin-to-orbital angular momentum conversion in inhomogeneous anisotropic media, *Phys. Rev. Lett.* **96**, 163905 (2006).
- [19] G. Vallone, A. Sponselli, V. D'Ambrosio, L. Marrucci, F. Sciarrino, and P. Villoresi, Birth and evolution of an optical vortex, *Opt. Express* **24**, 16390 (2016).
- [20] B. Sephton, A. Dudley, and A. Forbes, Revealing the radial modes in vortex beams, *Appl. Opt.* **55**, 7830 (2016).
- [21] J. Pinnell, I. Nape, B. Sephton, M. A. Cox, V. Rodríguez-Fajardo, and A. Forbes, Modal analysis of structured light with spatial light modulators: A practical tutorial, *J. Opt. Soc. Am. A* **37**, C146 (2020).
- [22] M. Mirhosseini, O. S. Magana-Loaiza, C. Chen, B. Rodenburg, M. Malik, and R. W. Boyd, Rapid generation of light beams carrying orbital angular momentum, *Opt. Express* **21**, 30196 (2013).
- [23] G. Vallone, Role of beam waist in Laguerre-Gauss expansion of vortex beams, *Opt. Lett.* **42**, 1097 (2017).
- [24] I. Nape, B. Sephton, Y.-W. Huang, A. Vallés, C.-W. Qiu, A. Ambrosio, F. Capasso, and A. Forbes, Enhancing the modal purity of orbital angular momentum photons, *Appl. Phys. Lett. Photon.* **5**, 070802 (2020).
- [25] F. Mei, G. Qu, X. Sha, J. Han, M. Yu, H. Li, Q. Chen, Z. Ji, J. Ni, C.-W. Qiu, *et al.*, Cascaded metasurfaces for high-purity vortex generation, *Nat. Commun.* **14**, 6410 (2023).
- [26] J. Harrison, W. T. Buono, A. Forbes, and D. Naidoo, Aberration-induced vortex splitting in amplified orbital angular momentum beams, *Opt. Express* **31**, 17593 (2023).
- [27] E. Brasselet, Babinet-bilayered geometric phase optical elements, *Opt. Lett.* **43**, 2623 (2018).